Copper Vanadate Nanobelts as Anodes for Photoelectrochemical Water Splitting: Influence of CoO_X Overlayers on Functional Performances

Leonardo Girardi, [†] *Gian Andrea Rizzi,**,[†] *Lorenzo Bigiani,*[†] *Davide Barreca,*[‡] *Chiara Maccato*,[†] *Carla Marega and Gaetano Granozzi*[†]

[†] Department of Chemical Sciences, Padova University and INSTM, 35131 Padova, Italy

[‡] CNR-ICMATE and INSTM, Department of Chemical Sciences, Padova University, 35131 Padova, Italy

* Author to whom correspondence should be addressed; E-mail: gianandrea.rizzi@unipd.it

ABSTRACT: The design and development of environmentally friendly and robust anodes for photoelectrochemical (PEC) water splitting plays a critical role for the efficient conversion of radiant energy into hydrogen fuel. In this regard, quasi 1D copper vanadates (CuV_2O_6) were grown on conductive substrates by a hydrothermal procedure and processed for use as anodes in PEC cells, with particular attention on the role exerted by cobalt oxide (CoO_x) overlayers deposited by radio frequency (RF)-Sputtering. The target materials were characterized in detail by a multi-technique approach, with the aim at elucidating the interplay between their structure, composition, morphology and the resulting activity as photoanodes. Functional tests were performed by standard electrochemical techniques like linear sweep voltammetry, impedance spectroscopy and by the less conventional intensity modulated photocurrent spectroscopy, yielding an important insight into the material PEC properties. The obtained results highlight that, despite the supposedly favourable band alignment between CuV_2O_6 and Co_3O_4 did not yield a net current density increase, cobalt oxide-functionalized anodes afforded a remarkable durability enhancement, an important pre-requisite for their eventual real-world applications. The concurrent phenomena accounting for the observed behavior are presented and discussed in relation to material physico-chemical properties.

KEYWORDS: copper vanadate, hydrothermal synthesis, nanobelts, cobalt oxide, photoelectrochemical water splitting, IMPS, LSV.

■ INTRODUCTION

The production of clean and sustainable energy from largely available and intrinsically renewable natural resources is one of the most important challenges to combat climate change and meet the ever-increasing energy demand of our planet. In this regard, an amenable alternative is the conversion of sunlight into chemical fuels, among which molecular hydrogen is regarded as the future energy carrier if the target of producing it efficiently and economically will be reached. A cost-effective and environmentally friendly technique to yield H_2 is photoelectrochemical (PEC) water splitting (WS)[1,2], but a current bottleneck for further developments is the anodic oxidation of water to O_2, a sluggish four-electron-transfer process with a significant energy barrier. To date, numerous semiconducting oxides (TiO_2,[3] Fe_2O_3,[4,5] WO_3,[6] $BiVO_4$,[7–9]) were fabricated and tested with the goal of producing a high-efficiency PEC-WS system for H_2 generation, but most of them suffer from a wide band gap and/or a fast electron-hole recombination rate and a limited durability[10]. To overcome these problems and increase the prospects of developing improved electrodes, nanomaterial engineering has involved the introduction of co-catalysts[11] or dopants,[12] the fabrication of tailored nano-architectures,[13] and the creation of heterojunctions.[14,15] As an example, Zhou *et al.* [16] prepared a heterojunction by growing on *n*-type Si(100) an overlayer of Co_3O_4, a well-known oxidation catalysts,[17] obtaining a dramatic enhancement in terms of both photocurrent and stability. This approach can be extended to other classes of materials like transition metal vanadates, as in the work by Chang *et al.*[18] where $BiVO_4$ PEC properties were significantly boosted by the modification with hydrothermally prepared cobalt oxide nanoparticles. Even copper vanadates, of general formula $Cu_xV_yO_z$, are an interesting class of materials featuring attractive PEC properties which can be finely tuned as a function of the Cu:V ratio.[19] In particular, an increase of the copper amount results in an improved absorption and charge separation, although at expenses of the charge transfer efficiency in solution, due to Cu^{2+} ions as acting as "hole trap" sites[19] In addition, it has been verified that the presence of a CuO_x layer prevents the corrosion of vanadium oxy-anions, as reported by Zhoue *et al.*,[20] reducing the detrimental decreases of the charge transfer efficiency with time. Among the various $Cu_xV_yO_z$ phases investigated

so far, the CuV_2O_6 phase has been somehow less studied, probably because it is particularly prone to photo-corrosion phenomena[20].

The main aim of the present work is thus to perform a tailored surface modification of CuV_2O_6, considered the best vanadate phase in terms of PEC activity,[21] in order to achieve an increase of functional performances and an improved photo-corrosion resistance. Similarly to the cases of $BiVO_4$ or Fe_2O_3,[8,18,22] herein the core idea is that of functionalizing the CuV_2O_6 surface with a thin Co_3O_4 overlayer, a *p*-type semiconducting oxide acting as very promising OER electrocatalyst.[17] The purpose of this strategy was to investigate whether, and to which extent, the following issues could contribute to the enhancement of material photoactivity and durability: i) the formation of *p-n* heterojuctions, to minimize detrimental charge carrier recombination; ii) the improvement of charge injection efficiency, taking advantage of the specific Co_3O_4 properties; iii) the suppression of detrimental material photo-corrosion phenomena. In this work, CuV_2O_6 nanobelt (NB) arrays fabricated by a simple and straightforward hydrothermal procedure were functionalized with CoO_x overlayers deposited *via* RF-sputtering, and finally thermal annealed in air. The use of RF-sputtering, at low temperatures and applied powers, in order to prevent undesired alterations of the underlying oxide matrix, has already been successfully exploited in combination with vapour phase techniques for the preparation of various multi-metal oxide-based nanostructures.[8,22] As a result, an intimate contact between the cobalt oxide overlayer and the pristine vanadate matrix can be obtained, an important point to benefit from the synergistic interplay between the single component properties.[17]

The obtained functionalized materials, which, to the best of our knowledge, have never been fabricated by the reported route up to date, were investigated in detail by means of various complementary techniques, devoting particular efforts to the impact of the system physico-chemical properties on the resulting PEC performances. The latter were investigated by linear sweep voltammetry with chopped light (chopped-LSV), electrochemical impedance spectroscopy (EIS) and by intensity modulated photocurrent spectroscopy (IMPS).[23,24] This last technique, typically used to characterize materials for photovoltaic devices, but much less commonly applied in the field of PEC-

WS,[13] allows to obtain accurate kinetic constants for charge recombination processes on the surface and charge transfer into the solution, thus allowing a detailed characterization of the intrinsic PEC properties of this material. Whereas in the case of other copper vanadates phases kinetic constants for charge recombination and charge injection efficiency have been measured by transient light measurements, no similar data for CuV_2O_6 or for the Co_3O_4/CuV_2O_6 systems are available in the literature up to date.

■ EXPERIMENTAL SECTION

Sample Preparation. The fabrication procedure adopted in the present study is sketched in Scheme 1. Copper vanadate nanobelts (NB) were prepared by hydrothermal growth on fluorine-doped tin oxide (FTO) glass slides (lateral dimensions = 1×1.5 cm) in a 23 mL Teflon Liner (Parr Instruments), pre-cleaned before use by sonication for 15 min in sequence in acetone, isopropanol and MilliQ water.

A 35 mM aqueous solution of ammonium vanadate (5 mL, 0.18 mmol) was prepared and stirred under heating up to 70°C to achieve a complete solid dissolution. As the solution became light-yellow, a 35 mM solution of copper sulphate pentahydrate (5 mL, 0.18 mmol) was added dropwise under a mild stirring, followed by the introduction of polyvinylpyrrolidone (0.02 g, average M.W. 8000 g/mol). After stirring for 15 min, the solution was transferred into a Teflon liner containing two vertically oriented FTO-glass slides. The vessel was maintained in an oven for 15 h at 180°C, and subsequently cooled down to room temperature in 1 h. After rinsing with MilliQ water, the samples were annealed in air at 450°C for 1 h.

The obtained systems were subsequently functionalized with cobalt oxide overlayers by means of RF-Sputtering, utilizing a custom-built two-electrode plasmochemical apparatus equipped with a RF generator (ν = 13.56 MHz). In particular, FTO-supported specimens were mounted on the ground electrode, whereas a cobalt target (99.95%, Alfa Aesar, thickness = 0.3mm) was fixed on the RF-electrode. Basing on previously optimized processing parameters,[17] experiments were performed from electronic grade Ar plasmas (flow rate =10 standard cubic centimetres per minute (sccm)), at a

growth temperature of 60°C, a total pressure of 0.3 mbar and a RF-power of 20 W. In order to tailor the overall Co amount in the resulting composites, two different sputtering times (1 h, 2 h) were used, as well as two different annealing temperatures (350°C and 200°C) to recover the oxidation state of the cobalt ions since the Co source was a metallic target. The samples were then subjected to thermal annealing in air under different conditions. In the following, samples are denoted as **NB** (bare copper vanadate, annealed in air at 450°C for 1h) and **NB+Xh Y°C** (copper vanadate nanobelts + CoO_x RF-sputtering for X h with X = 1, 2 h and a further annealing treatment at Y°C). In particular, the optimal annealing temperature for the CuV_2O_6 NBs was found to be 450°C. Higher annealing temperatures completely destroyed the NB morphology and possibly led to a decomposition of the vanadate into V_2O_5 and CuO, as verified by Raman analysis. If the annealing procedure (as grown-CuV_2O_6 + CoO_x) was carried out after the CoO_x deposition, we obtained a significant interdiffusion of the Co^{2+} ions into the CuV_2O_6 lattice as verified by X-ray photoelectron spectroscopy (XPS) analysis. Therefore, the optimal preparation procedure enabling to preserve the NB morphology and to minimise interdiffusion, was found to be a “2-step” annealing treatment. The first step, carried out at 450°C, was performed only on the CuV_2O_6 NB after the hydrothermal synthesis. The second step (200°C or 350°C) was performed on the CuV_2O_6 NBs after CoO_x decoration.

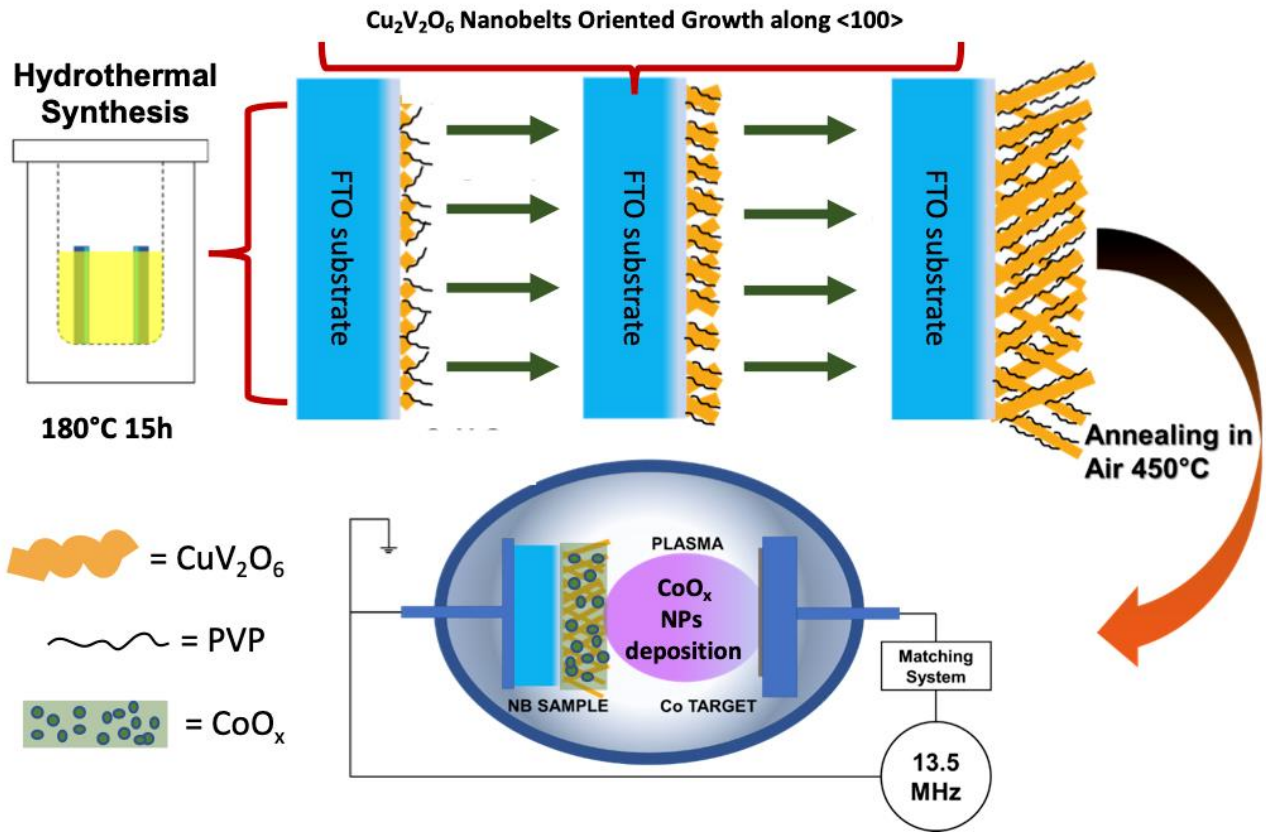

Scheme 1. Schematic representation of the procedure adopted in the present study for the fabrication of $Cu_2V_2O_6$ nanobelts (NB) and their functionalization with CoO_x overlayers.

Physico-chemical Characterization. Field emission-scanning electron microscopy (FE-SEM) and energy dispersive X-ray spectroscopy (EDXS) analyses were carried out by means of a Zeiss field-emission SUPRA 40 VP instrument equipped with an INCAx-act PentaFET Precision spectrometer (Oxford Instruments), using primary beam acceleration voltages between 10 and 20 kV. The average nanoaggregate sizes were evaluated by a statistical analysis of the obtained micrographs using the ImageJ® software.

XPS measurements were performed on a custom-built ultra-high vacuum (UHV) chamber (base pressure = 5 x10^{-10} mbar) equipped with a non-monochromatized double-anode X-ray source (Omicron DAR-400, Scienta-Omicron GmbH, Uppsala, Sweden), a hemispherical electron analyzer (Omicron EA-125; acceptance angle = ± 4°) and a 5-channeltrons detection assembly. The diameter of the analysed area was 3 mm. The spectra were acquired using the AlK_α radiation (hν = 1486.6

eV). The binding energy values were calibrated by using the position of the adventitious C1s line at 284.7 eV. Data analysis involved Shirley-type background subtraction and peak area determination by integration, using, where necessary, non-linear least-squares curve fitting adopting Voigt peak shapes. Atomic compositions were evaluated from peak areas using sensitivity factors supplied by Yeh.[25]

Wide angle X-ray Diffraction (XRD) patterns were recorded in the diffraction angular range 10 – 80° by a PANalytical XPERT-3 diffractometer, working in the reflection geometry and equipped with a graphite monochromator on the diffracted beam (CuKα radiation, Pananlytical, Almelo, The Netherlands). The analysis of XRD patterns was carried out by using the HighScore Plus[26] software

Raman spectra were acquired in air by means of a Thermo-Fisher DXR Raman microscope using a 532 nm laser (1 mW), focused on the sample with a 50x objective (Thermo-Fisher Scientific, Madison, WI, USA) obtaining a spot size of about 1 μm. An investigation performed by collecting additional spectra in different region of the samples demonstrated that they were homogeneous on a micron scale.

Optical spectra were acquired in absorbance and reflectance mode on a UV–Vis Cary 5E spectrophotometer, operating in air in transmission mode at normal incidence. In each spectrum, the FTO substrate contribution as subtracted. Band gap energies (E_G) were extrapolated by applying the Tauc method.[27]

Photoluminescence spectra were recorded, in front face acquisition geometry, with a Horiba JobinYvon Fluorolog-3 spectrofluorimeter equipped with double-grating monochromator in both the excitation and emission sides coupled to a R928P Hamamatsu photomultiplier and a 450 W Xe arc lamp as the excitation source. Emission spectra (λ_{exc} = 420 nm) were corrected for detection and optical spectral response of the spectrofluorimeter supplied by the manufacturer.

Functional tests. PEC tests were carried out in a 0.1 M Na borate buffer solution (pH = 9.3) prepared dissolving sodium borate (Sigma Aldrich, 99%) in MQ water. The measurements were conducted in a Teflon PEC cell provided by PINE Research Instrumentation (2741 Campus Walk Avenue Building

100 Durham, NC 27705 USA) with the samples mounted outside the cell and kept in position by an O-ring seal. A Pt wire and Ag/AgCl electrode (0.212 *vs.* Reference Hydrogen Electrode (RHE)), were used as counter electrode and reference electrode, respectively. Illumination was performed using a 100 mW/cm^2 (neutral white – Philips LUMILEDS) light emitting diode (LED) source controlled by the optical bench (Metrohm-Autolab) coupled to the Autolab PGSTAT204 (Metrohm, Utrecht, The Netherlands) instrument. Incident Photon Conversion Efficiency (IPCE) tests were performed using LED sources (Philips LUMILEDS) with emission wavelengths at: 470, 505, 530, 590, 617, 627, 655 nm. Each led intensity was measured separately by a photodiode (FDS100). The same potentiostat was used to perform the EIS and Mott-Schottky analysis, in the 10^5-10^{-1} Hz frequency range. This instrumentation and the led driver were used to perform also IMPS measurements for several potential values of (1.05-1.75 *vs.* RHE) in the frequency range from 20 kHz to 0.05 Hz, with a constant light intensity of 50 mW/cm^2 and a modulation with an amplitude of 2 mW/cm^2, adjusted in order to have a linear response (the EIS frequency generator was used to drive the led pulses). Andrea questa frase si puo' togliere o è il caso di lasciarla? The kinetic constants and charge injection efficiency were all determined from the Nyquist plots of IMPS data after normalization procedure [11].

■ RESULTS AND DISCUSSION

Material characterization. The possibility to form an useful *p-n* junction was verified by preliminary experiments where we deposited small quantities of Co_3O_4 nanoparticles (prepared by the hydrothermal method[18]) on the CuV_2O_6 sample obtained by hydrothermal growth on FTO (see Experimental Section Figure S1a-d) . The Mott-Schottky plot (Figure S1c), obtained from this sample after a mild annealing at 100°C, presented a favourable alignment of Co_3O_4 and CuV_2O_6 valence band (VB) and conduction band (CB), respectively (Figure S1d). The sample modified with cobalt nanoparticles was also tested by photoluminescence, to verify the beneficial effect of the cobalt in terms of charge separation. Indeed, Figure S1b shows that material luminescence after the surface treatment almost disappears. These encouraging results prompted us to perform the deposition of

CoO_x overlayers in a more controlled way by using RF-sputtering as described in the experimental section.

The morphology of CuV_2O_6 samples was investigated by FE-SEM analyses (Figure 1 and Figure S2) both immediately after deposition and the annealing process. As can be observed, the as prepared samples consist in an array of nanobelts (NB), about 200 nm wide and about 3 μm long. These nano-architectures, often obtained by hydrothermal deposition, are useful because of their high surface area and of their oriented growth along a preferential direction, which entails the formation of tiny single crystals with a low amount of grain boundaries and defects, that usually act adversely as recombination centres[28,29]. As a consequence, such a sample should in principle possess promising PEC properties. After the annealing process, the NBs become thicker with more rounded edges, and their crystallinity increased (see XRD in Figure S3), in line with previous results on FTO-supported iron oxide nanosystems[5]. The morphology of the samples decorated by CoO_x is almost identical, as clearly seen in Figure 1d-f, thanks to the relatively mild plasma conditions utilized in the present RF-Sputtering process. The presence of CoO_x "nano-petals" on top of the NB is also visible (Figure 1e-f).

It is worthwhile noting that the attainment of the NBs is directly influenced by the chemical composition of the starting solution. In fact, in the absence of PVP as a template-directing agent, no NBs could be obtained. In addition, a Cu:V ratio of 1:2 instead of 1:1 yields the formation of wider NBs, but the coverage of the FTO substrate is very low (Figure S4).

Preliminary information on the system chemical composition was obtained by EDXS mapping providing interesting insight into the spatial distribution of the different elements. The representative results are summarized in Figure 2. The data clearly show an even distribution of Cu, O and V throughout the sampled area, in line with the uniform formation of copper vanadate and an even dispersion of cobalt over the analyzed area. The estimated Co/V percentage ratio was 1/60.

Cross-sectional EDXS line-scan map (Figure S2c) shows that Cu and V traces have an analogous trend along the whole profile, thus confirming their common chemical origin. As regards to cobalt,

its curve indicated a uniform distribution as a function of depth, suggesting an uniform coating of the CuV_2O_6 nanostructures by the RF-Sputtered CoO_x overlayer, in line with previous results.[17]

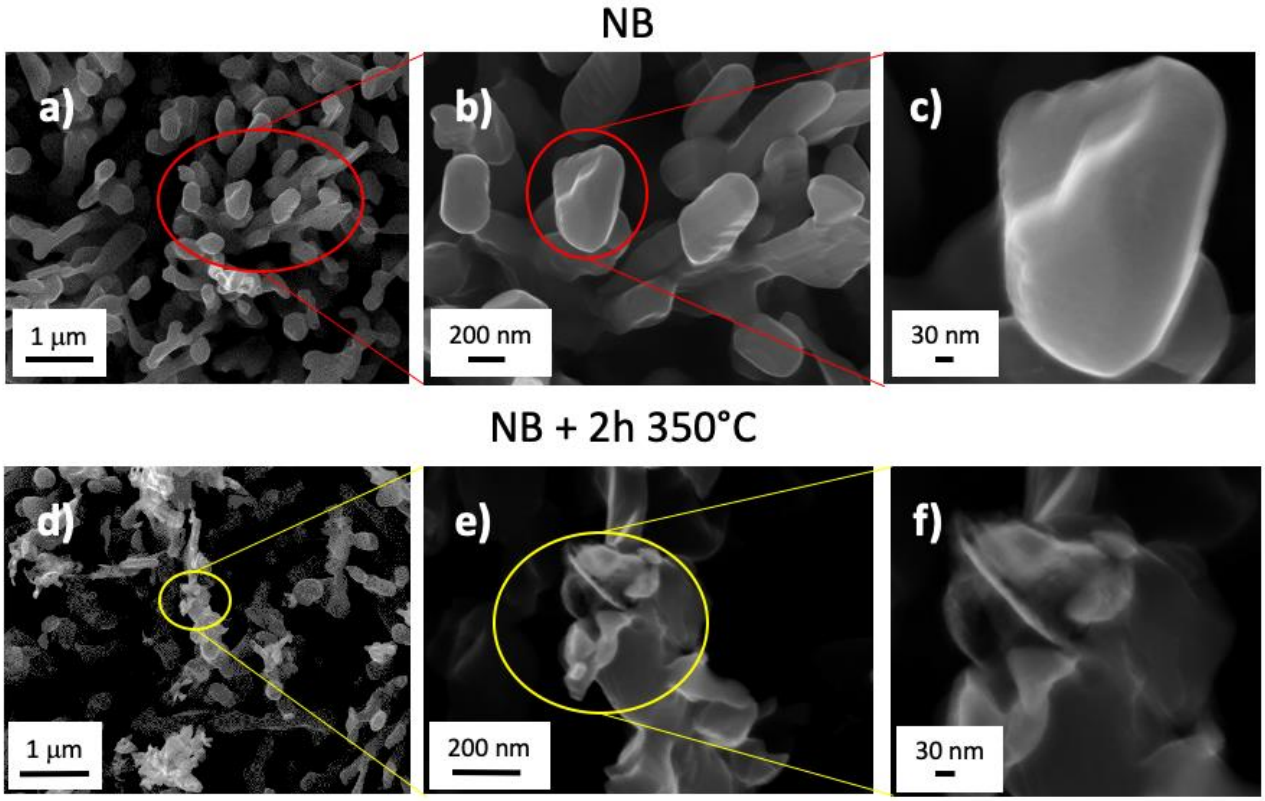

Figure 1. FE-SEM images for: (a-c) the NB specimen after annealing in air at 450°C for 1 h; (d-f) NB + 2 350°C.

Raman spectroscopy was used for a preliminary analysis of material composition. As shown in Figure 3, the collected spectra present peaks that can all be assigned to the CuV_2O_6 phase. The main peak at 904 cm^{-1} was related to the stretching mode of V-O.[30] The other signals are typical of the vanadium oxide phases, and are assigned to different vibrational modes of the V-O network, modified with respect to V_2O_5 by the presence of copper species.[30] In the case of samples functionalized with CoO_x, it was impossible to observe signals that could be assigned to either Co_3O_4 or CoO_x probably due to their very low amount (see below).

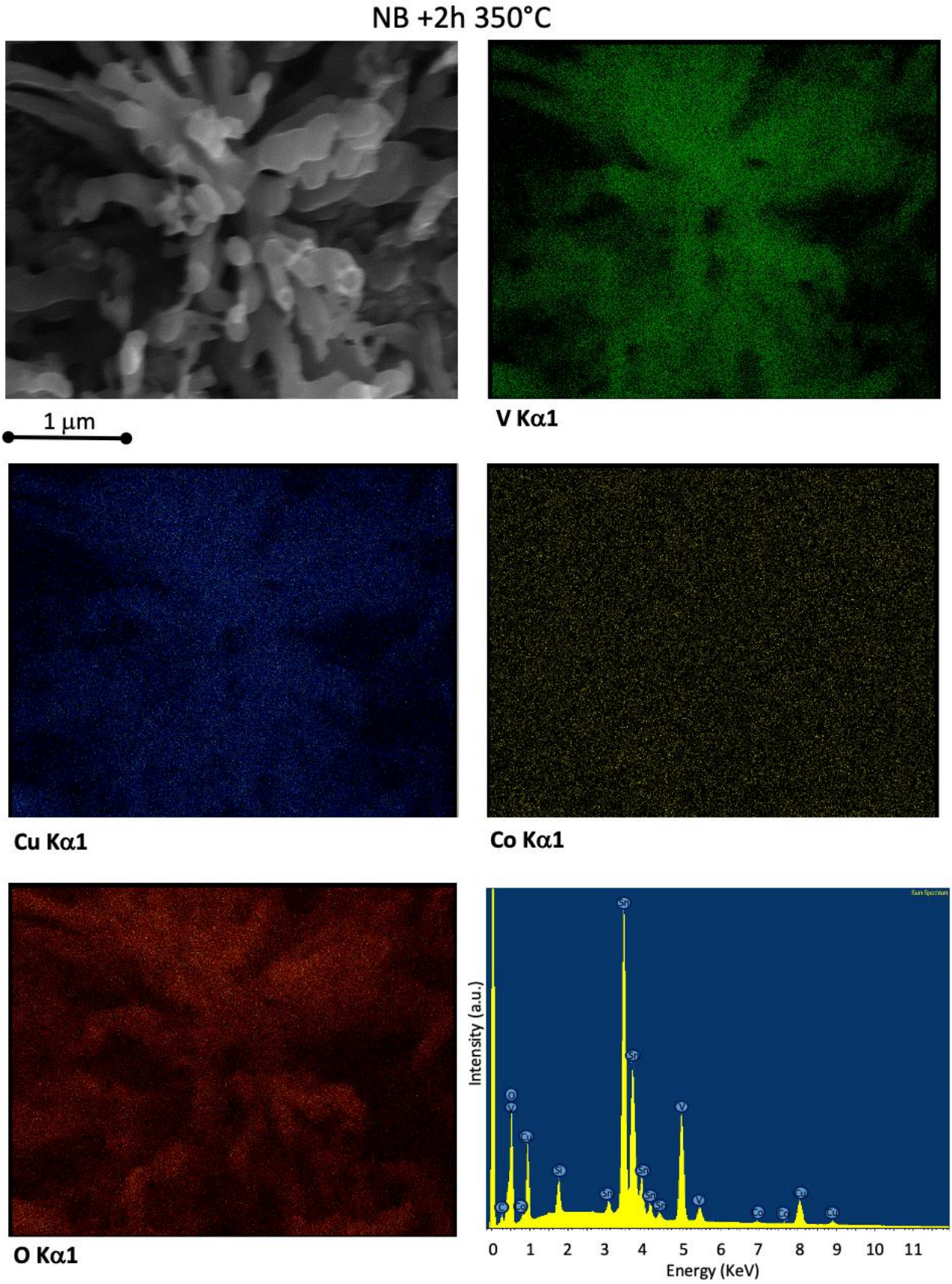

Figure 2. EDXS spectrum and corresponding chemical maps acquired in area of the upper left FESEM image for sample NB + 2h 350°C.

Structural analyses were performed by means of XRD (Figure 3). Before functionalization, the sample pattern was characterized by reflections located at 2θ = 20.7°, 26.8°, 27.7°, 29.4°, 29.5°, and 31.7°, corresponding to the (011), (100), (110), (01-1), (012), (101) reflections of the CuV_2O_6 triclinic phase.[31] A weak peak was also detected at 2θ = 24.7° and assigned to the presence of small amounts of the monoclinic β-$Cu_2V_2O_7$ phase[32] (*ziesite*), whose occurrence was tentatively ascribed to its nucleation in solution, with subsequent adsorption on the CuV_2O_6 NB. A further analysis of the relative peak intensities in comparison to the reference powder spectrum revealed that the CuV_2O_6 reflection at 2θ = 27.7° (110) was the most intense, suggesting thus a preferential growth along the <110> direction. A detailed analysis of XRD patterns indicated that the sample is composed by 86% w/w (98% molar) of CuV_2O_6, the remaining 14% being the β-$Cu_2V_2O_7$ phase. Upon functionalization with CoO_x, no significant variations take place, a phenomenon ascribed to the very low amount (and thickness) of the deposited cobalt oxide.

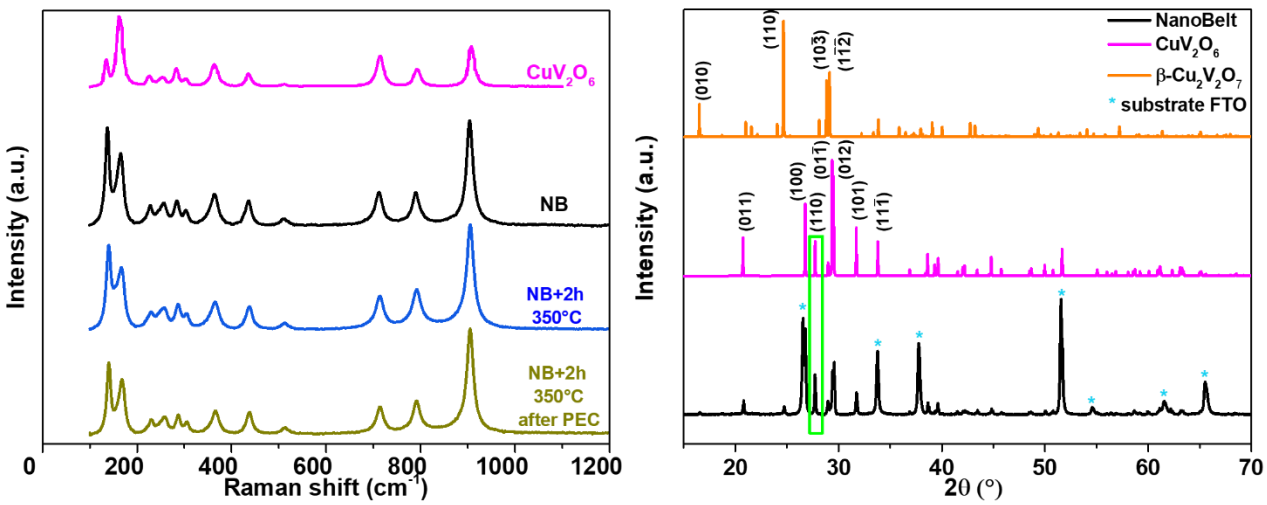

Figure 3. Raman spectra of the CuV_2O_6 Nanobelt sample (black), NB + 2h 350°C CoO_x before (blue) and after (dark cyan) the PEC tests and the reference spectra (pink) . On the right side there are the XRD spectra of the NB sample (black) and the FTO glass (cyan) and the reference spectra for the β-$Cu_2V_2O_7$ (orange) and CuV_2O_6 (pink) phases.

The preferential growth of the CuV_2O_6 phase on the FTO substrate can be ascribed to the good matching between the (110) planes of SnO_2 (tetragonal, space group: $P4_2/mnm$) and the (110) planes of CuV_2O_6 (triclinic, space group: $P\bar{1}$), the theoretical mismatch being only 4%. The growth mechanism likely involves the initial nucleation process of the CuV_2O_6 phase on FTO, followed by the anisotropic growth due to PVP adsorption[33].

The above observations, evidence that the best results corresponded to a Cu:V = 1: 1 ratio in the starting solution. Basing on the CuV_2O_6 stoichiometry, this suggested the occurrence of a Cu^{2+} excess in the working solution, as supported by the UV-Vis spectra of the solution after the reaction (Figure S5).

Important information on the surface composition are also obtained by XPS spectroscopy, before and after PEC measurements (Figure S6). Spectral deconvolution of the Cu $2p_{3/2}$ region (Figure 4) revealed the presence of Cu^{2+} (BE= 933.7 eV), Cu^{+} (BE = 933.2 eV), as well as Cu^{2+} hydroxide (BE = 935.1 eV).[15] As concerns the V 2p peak, only the presence of V^{5+} species (BE = 516.7 eV) are observed, and no other components could be assigned to other vanadium oxidation states (Figure S7). After deposition of RF-sputtered CoO_x on the CuV_2O_6 NBs, the shape and position of the XPS Co 2p peak (Figure S8) were in line with the presence of CoO as the main species[34], and the annealing procedure did not yield significant variations in the Co oxidation state. On the other hand, the Co modified Auger parameter (Figure S8 lower panel), calculated as reported in [35], (1553.2, 1552.4 and 1551.3 eV for NB 1h as prepared, NB 1h and NB 2h, respectively) is compatible with both Co_3O_4 and CoO [36]. For this reason, we think that the cobalt oxide coating should be better identified as CoO_x consisting in a mixture of CoO and Co_3O_4. As shown in Figures 4b-c, the Cu^{+} component (BE = 933.2 eV) underwent a significant intensity enhancement in the CoO_x-coated samples, indicating the occurrence of a concomitant $Cu^{2+} \rightarrow Cu^{+}$ partial reduction. The Cu^{+} component was clearly visible also after annealing in air at 350°C, indicating that the CoO_x-coated samples are characterized by the presence of oxygen vacancies in the CuV_2O_6 lattice. In fact, the charge electroneutrality in the lattice can be maintained by one oxygen vacancy every two Cu^{+} sites.

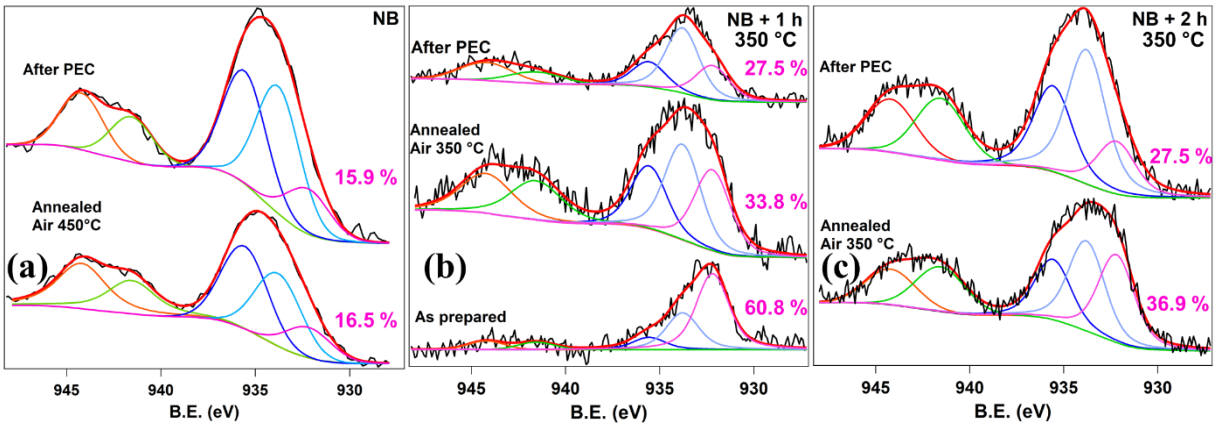

Figure 4. XPS Cu $2p_{3/2}$ spectral region of the different studied samples before and after PEC tests. In pink are reported the atomic percentage of $Cu^{+}$for each sample.

Photoelectrochemical characterization. A preliminary screening of PEC functional properties revealed that the best photoactivities correspond to samples coated by RF-sputtered CoO_x for 1 and 2 h, and annealed in air at 200°C and 350°C. In the following, the attention will be focused on the results pertaining to these specimens.

Chopped linear sweep voltammetry (LSV) measurements (Figure 5a) reveals that the pristine CuV_2O_6 material yields the best performances in terms of photocurrent density and photocurrent onset. The curves showed the classical "square wave" shape with spikes when the LED is switched on and off. This rapid increase of the photocurrent when the light is turned on is due to the instantaneous generation of carriers (see scheme in Figure 6) that, as time passes, are progressively quenched by trap states and by the recombination with the majority carriers [23] (electrons).

When the LED is turned off, the minority carriers (holes) that were trapped with the light on, are "de-trapped" and this causes the change in the sign of the current (cathodic spikes). It is possible to observe that some more intense cathodic spikes were also present at ≈1.4 V *vs.* RHE and that they were modulated like a voltammetry peak. This behaviour could be related to surface states[37] that are populated during illumination and that, when the light is switched off, release the trapped charges (holes) in the material causing an instantaneous negative current.

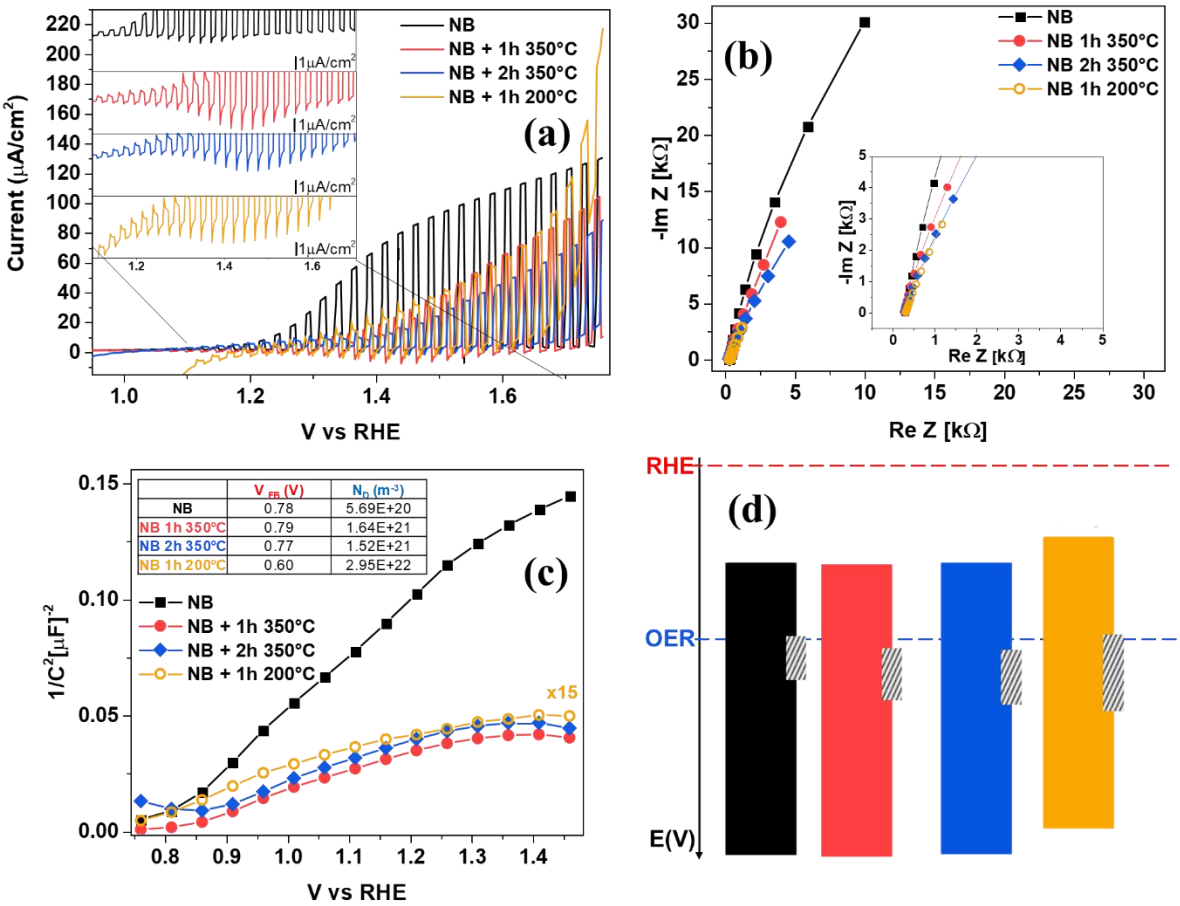

	V_{FB} (V)	N_D (m^{-3})
NB	0.78	5.69E+20
NB 1h 350°C	0.79	1.64E+21
NB 2h 350°C	0.77	1.52E+21
NB 1h 200°C	0.60	2.95E+22

Figure 5. (a) Chopped light linear sweep voltammetries in NaBi buffer solution (scan rate = 5 mV/s; chopping frequency = 0.4 Hz). An enlarged zone of the cathodic spikes is displayed in the inset. (b) EIS spectra at 1.4 V vs RHE in the 10^5- 0.1 Hz frequency range. (c) Mott-Schottky plots of the target specimens. Majority carriers concentrations are reported in the inset. (d) Approximate band edges position as obtained from Mott-Schottly plots. The white rectangles with black stripes represent the position and the potential width of the cathodic spikes observed in the chopped LSV curves.

The target samples were also characterized by electrochemical impedance spectroscopy (EIS) acquired at 1.4 V *vs.* RHE. EIS spectra (Figure 5b) show that functionalization of the pristine systems with CoO_x lowers the material charge transfer resistance. The corresponding Mott-Schottky plots (Figure 5c) highlight the occurrence of a *n*-type conductivity for all the analysed samples. At variance with the preliminary tests obtained upon coating CuV_2O_6 surface with pre-formed Co_3O_4 nanoparticles by drop-casting (see Figure S1), no apparent *p-n* junction formation could be unambiguously observed. Indeed, a very pronounced change in the slope of the $1/C^2$ curve of the

coated samples was also visible. Since the slope value is proportional to the reciprocal free carrier concentration,[15] these results highlight that the functionalized samples were characterized by a much higher free carrier concentration, directly influenced by the amount of deposited CoO_x and the used annealing temperature. At the same time, the *x*-axis intercept did not show significant variations, indicating that the flat band potential (V_{fb}) was unchanged, except for the sample annealed at 200°C. In fact, the latter clearly showed a lower V_{fb} value and a much higher donor concentration. It is also evident that the photocurrent onset changes with the surface modification, passing from 1.2 V for the NB sample to 1.4 V, 1.4 V and 1.3 V for the samples 1h 350°C, 2 h 350°C, and 1 h 200°C, respectively. The onset values were shifted from the flat band potentials, suggesting that the target specimens are characterized by a pinning effect of the Fermi level.[38,39]

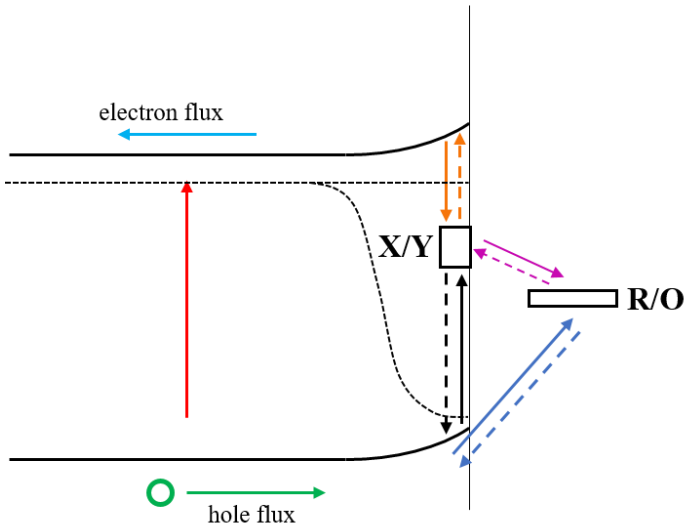

Figure 6. Scheme of charge dynamics that take place in photoanode at the interface with an electrolyte with a redox couple (R-O). In the scheme, the mechanism for holes and electrons trapping (X/Y), and the charge transfer in solution from the valence band and from the surface states is indicated by the arrows.

From the V_{fb} values, the VB and CB potentials could be positioned with respect to the RHE scale. Usually, the position of the conduction band (CB) is ≈0.1 eV more negative[21] than the flat band potential (for a *n*-type semiconductor), so that the VB position is simply found by adding to CB the value of optical energy gap measured by UV-Vis diffuse reflectance spectra (≈1.8 eV, Figure S9). In

this band diagram we represent, as white rectangles with black stripes, the position of the cathodic spikes that are observed in the chopped LSV. As explained below, these rectangles represent "trap-states". The Mott-Schottky plots showed a higher carrier concentration in the samples functionalized with CoO_x, whereas XPS showed the presence of Cu^+ and Co^{2+} centres on material surface. A rationale accounting for these observations is based on the involvement of Cu^+ and Co^{2+} centres in the increase of the carrier concentration through creation of oxygen vacancies. A possible mechanism taking into account the ion interdiffusion between the two oxides (CuV_2O_6 and CoO) could be:

$$\mathrm{CuV_2O_6} + \frac{x}{2}\mathrm{Co} \rightarrow \mathrm{Cu(II)}_{[1-x]}\mathrm{Cu(I)}_x\mathrm{V_2O}_{[6-\frac{x}{2}]} + \frac{x}{2}\mathrm{CoO} \quad \textbf{(1)}$$

$$\mathrm{Cu(II)}_{[1-x]}\mathrm{Cu(I)}_x\mathrm{V_2O}_{\left[6-\frac{x}{2}\right]} + z\mathrm{CoO} \xRightarrow{\text{Annealing}} \mathrm{Cu}_{[1-x-z]}\mathrm{Co(II)}_z\mathrm{Cu(I)}_x\mathrm{V_2O}_{[6-\frac{x}{2}]} + z\mathrm{CuO} \quad \textbf{(2)}$$

It is worth noticing that the above reported mechanism is in agreement with the very close value ionic radii for Co^{2+} and Cu^{2+} (88 and 87 pm)[40], respectively implying also the formation of a CuO layer on material surface, after annealing. At high sample bias, Cu^+ and Co^{2+} centers can be partially oxidized to Cu^{2+} and Co^{3+}, respectively. As the light is turned on, photogenerated electrons can be trapped on these sites, with a consequent lowering of carriers available for the charge transfer. Finally, we report in the SI, Figure S10 the IPCE acquired for samples NB and NB 2h 350°C. It is interesting to notice that in this last case at low bias (1.2 V *vs.* RHE), an improvement for wavelengths > 550 nm is registered. In order to better understand the role of the cobalt oxide and to quantitatively measure the charge transfer efficiency, a systematic analysis of all specimens was performed IMPS.[11,23,24] IMPS is a technique that probes the system with a time modulated light intensity (p(ω)) that produces a time dependent photocurrent (j(ω)). A transfer function of the system (H(ω) = j(ω)/p(ω)), that depends from the frequency of the modulation, can be obtained from these input and output signals. This function yields information about the charge-carriers dynamics on the material surface and allows to

calculate the efficiency of charge transfer (η_{CT}) and the kinetic constants of charge transfer (k_{CT}) and recombination processes (k_{rec}).

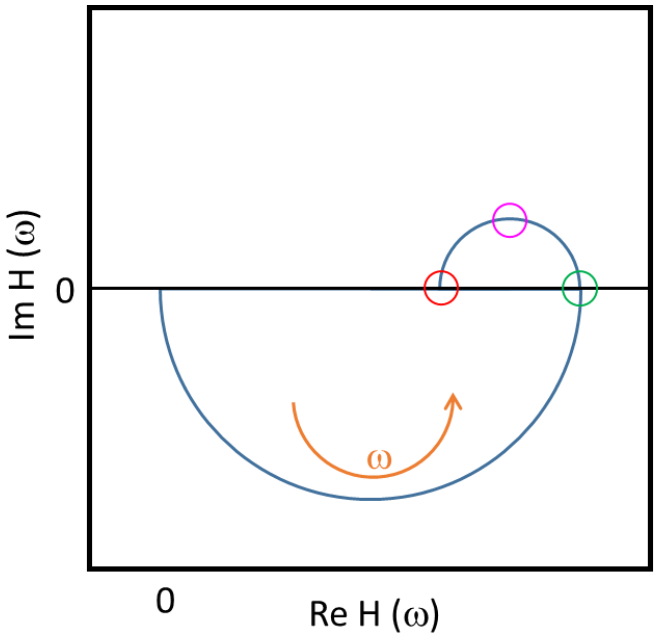

$$H(\omega) \propto \frac{k_{CT} + i\omega}{k_{CT} + k_{rec} + i\omega}\left[\frac{1}{1 + i\omega\tau_c}\right]$$

$$\eta_{CT} = \frac{LFI}{HFI} = \frac{k_{CT}}{k_{rec} + k_{CT}}$$

$$\omega_{ImH \to MAX} = k_{rec} + k_{CT}$$

Figure 7. Typical IMPS plot for a photoanode, where H is the transfer function of the system defined as $H(\omega) = j(\omega)/p(\omega)$. The equations that allow the fitting of the plot and the calculation of kinetic constants are reported on the right side of the figure.

In the case of a semiconductor working as a photoanode, an IMPS plot, like the one reported in Figure 7, can be interpreted using the model proposed by Ponomarev,[24] considering a *n*-type semiconductor with surface states that can participate to the charge transfer process. The typical IMPS plot displays the imaginary part *vs*. the real one, and it is formed by two semicircles in the cartesian coordinate system, one in the fourth quadrant and the second in the first quadrant of the complex plane. The negative semi-circle is related to the capacitive response of the cell and the frequency corresponding to the minimum of the curve is directly related to the time constant of the apparatus used in the measurement. The second semi-circle (in the first quadrant) is related to the recombination and charge transfer processes of minority carriers (in this case, holes). The high frequency intercept (HFI) is closely related to the flux of holes generated upon illumination, as calculated by the Gärtner equation[23,41], before recombination processes occur. The maximum theoretical hole density is

reduced due to trapping and recombination events, so that only a lower amount can be transferred to the solution. These phenomena have a time dependence (kinetic constants of the process) and, when the perturbation becomes slow enough to activate the process, it is possible to observe an increase in the imaginary part of H (related to the loss of minority carriers) until ω_{max} is reached (purple circle on Figure 6). As the frequency reaches lower values, the system, already stabilized, decreases the loss of minority carriers, and at very low frequency the imaginary part becomes zero. The low frequency intercept (LFI) represents the maximum photocurrent that can be observed taking into account loss processes. This means that the charge transfer efficiency can be calculated simply by the ratio of this intercept (LFI) with the real axis, divided by the high frequency intercepts (HFI). The calculation of k_{rec} and k_{CT} can be easily obtained from the equations reported in Figure 7:

$$k_{CT} = \omega_{Max}\frac{\mathrm{LFI}}{\mathrm{HFI}} \qquad \mathrm{k_{rec}} = \omega_{max} - \mathrm{k_{CT}} \tag{1}$$

In fact, the LFI/HFI and ω_{max} values are directly obtained from the IMPS plot after normalization procedure as described in the caption of Figure S11. It is important to point out that the PEC performances obtained from an IMPS analysis are independent from the electrochemical area that, in the case of supported nanosystems, is difficult to be directly measured. These values are therefore intrinsic properties of the material with that particular nanostructure (nanobelts). Finally, we can point out that the kinetic constants values can also be obtained by fitting the IMPS curve with a suitable model, although this procedure is strongly complicated by the asymmetry of the semi-circles as discussed above. Therefore, in our case all the data reported in Figure 6 have been computed from the values of η_{CT} and ω_{max}.

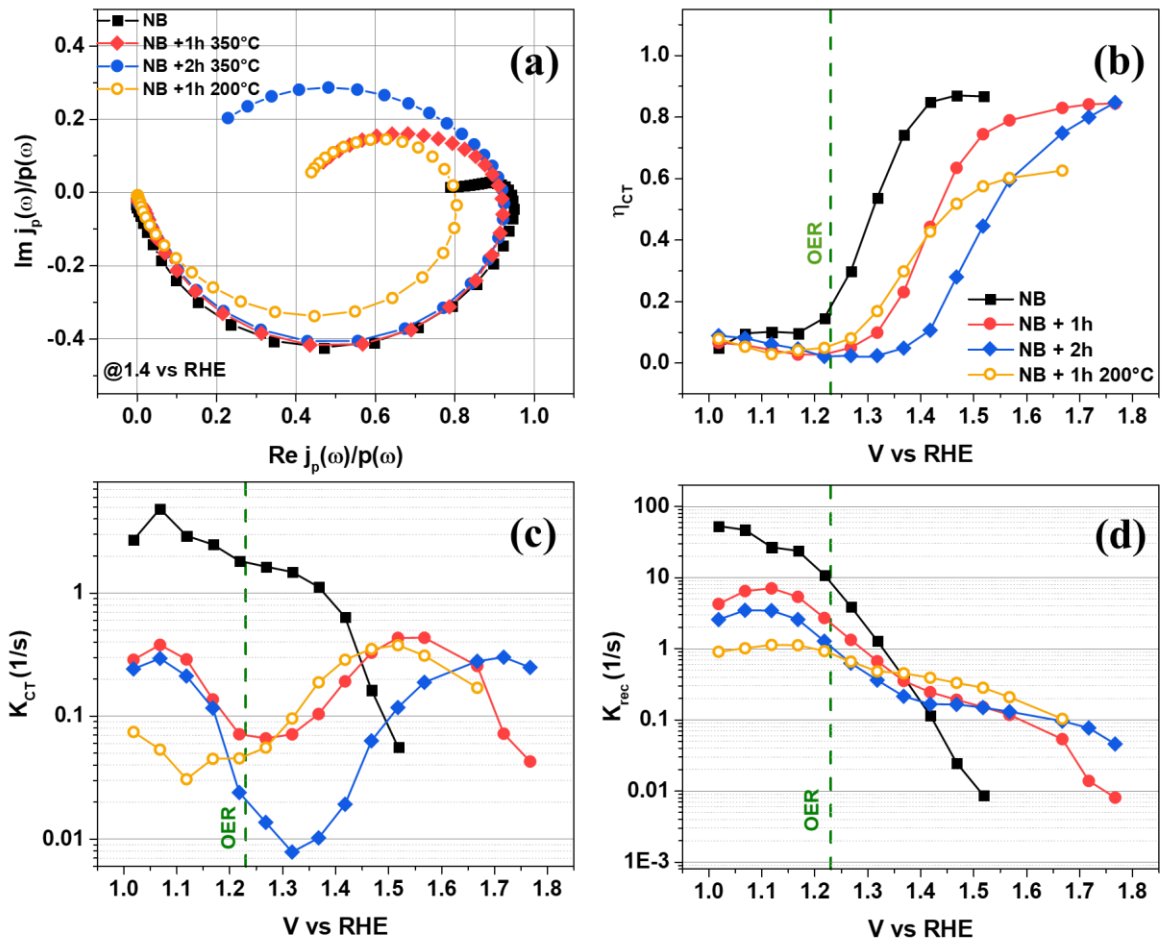

Figure 8. (a) IMPS Nyquist plots of the measured transfer functions at 1.4 V *vs*. RHE. (b) Charge transfer efficiency as a function of the applied potential for the different samples. (c) Charge transfer and (d)recombination (d) kinetic constants as function of the applied bias.

The results of the IMPS analysis are summarized in Figure 8, while the whole set of Nyquist plots is reported in Figure S11. The obtained data show that the pristine material (CuV_2O_6) yields the best OER characteristics in terms of a higher charge-transfer kinetic constant at low potentials. The CoO_x-functionalized samples present a lower k_{ct} value at 1.4 V *vs*. RHE. The k_{ct} curve minimum corresponds to the presence of "trap-states", as previously discussed. These "trap states" do not completely prevent charge transfer processes, but they slow down the whole process. Conversely, for bias values higher than 1.4 V *vs*. RHE, the CoO_x-functionalized specimens yield an activity comparable to, or higher than, the pristine CuV_2O_6. It is worthwhile observing that the HFI

dependence on potential should follow the Gärtner equation, that predicts a photocurrent density saturation at high bias values (Figure S12). Figure 9, displays the chopped LSVs before and after IMPS measurements, highlighting the completely different behaviour of CoO_x-functionalized samples. Only the CuV_2O_6 NB sample shows a clear slope change due to the achievement of a high external quantum efficiency (EQE), whereas the other samples still yield high recombination losses. In the present case, the IMPS curves are acquired from low to high bias, meaning that the high bias curves are obtained after 5-6 h of photoelectrochemical work. After that test, the photocurrent of the pristine material practically disappeared, while for the sample obtained after a CoO_x deposition of 2 h almost no change took place.

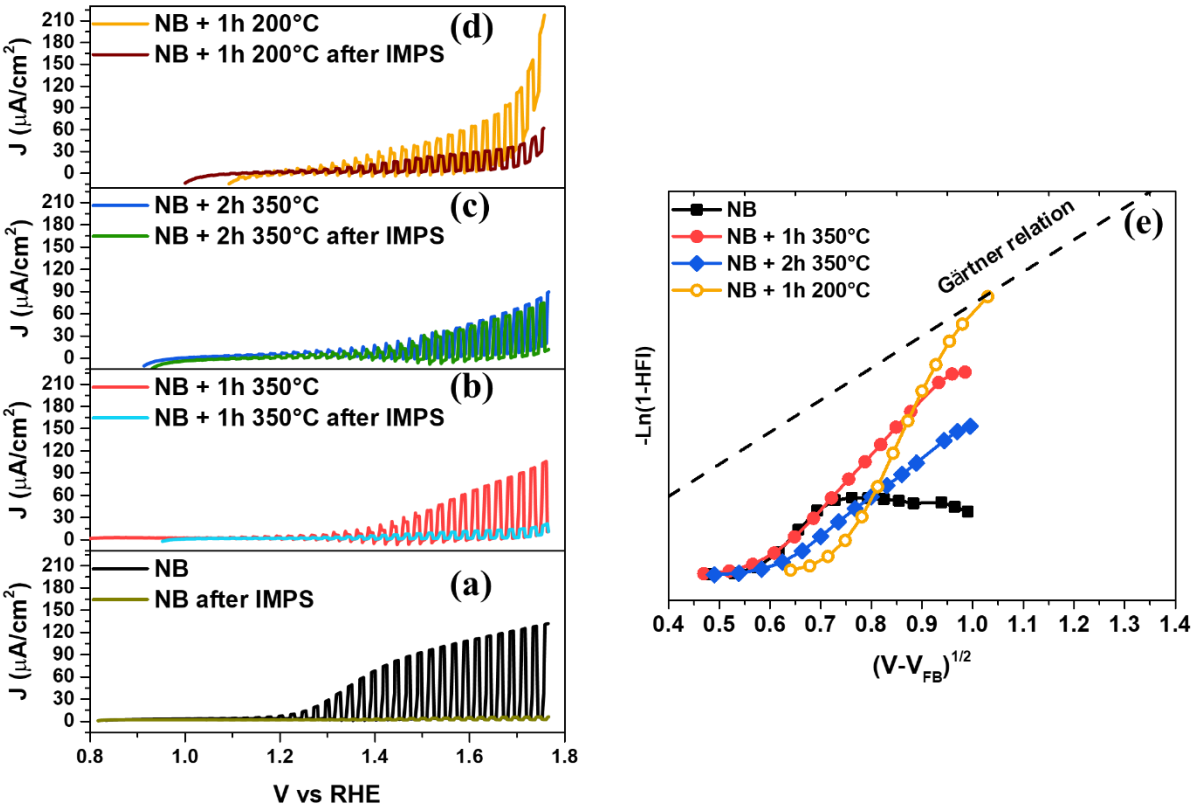

Figure 9. (a, b, c, d) Chopped LSVs for the target samples before and after IMPS measurements. (e) Gärtner relation dependence on the band bending in comparison to the presently obtained experimental data.

Figure 9e compares the experimental HFI with the Gärtner equation, evidencing different trends for the analysed specimens. In particular, only the bare CuV_2O_6 NB showed a saturation with a little

decrease, indicating a low charge carrier recombination. Nevertheless, the corrosion becomes subsequently predominant, causing a decrease in the material amount that can absorb the photons and in consequence the amount of photogenerated holes (value described by HFI). In fact, the black dots curve in Figure 9e shows a slowly decreasing plateau. In a different way, the functionalized samples show a dependence clearly related on recombination process even at high band bending. The improved performances obtained for CuV_2O_6 in terms of durability are likely due to the formation of the CuO passivating layer induced by Co^{2+} ions interdiffusion at the interface. This layer should prevent, as already observed in the case of $Cu_3V_2O_8$[20], the loss of V^{5+} in the electrolyte as $H_2V_2O_6$ and related oxo-anions, a process usually occurring in the case of transition metals vanadates [20]. The formation of the CuO layer is explained in reactions 1 and 2 and further confirmed by the XPS data reported in the SI (Figure S5). A better adhesion of the CuV_2O_6 NB with the substrate could, in principle, be achieved after the two consecutive thermal treatments adopted in the preparation procedure, but the occurrence of an oriented crystal growth on the FTO substrate (see XRD data) testifies the achievement of a solid adhesion already during the hydrothermal process. Although this layer does not bring about an increase in material photoactivity, its stability is strongly enhanced, which is an important pre-requisite in view of eventual practical end-use. The obtained result is successful in terms of an improved system durability, but, at the same time, the obtained data suggested the obtainment of a doping rather than the formation of *p-n* junctions., This conclusion is corroborated by Mott-Schottky plots, that highlight an *n*-type conductivity with majority carrier concentration increasing proportionally to the deposited CoO_x amount. Finally, it is interesting to compare our results with those previously obtained by other authors on analogous materials (Table S1, SI). It is worthwhile observing that, in the study published by Jiang *et al.*,[19] the kinetic constants were obtained by pulsed light measurements (constant white light illumination + blue light pulses) and all the reported values (k_{rec} and k_{CT}) are systematically higher than the ones obtained in the present study. A comparison with photocurrents onset values and photocurrent densities shows that the performances of the pure CuV_2O_6 NB reported in the present study are comparable with those of

other vanadate phases studied by Jiang and by Guo.[21] Although the different way in which the kinetic constants are determined (pulsed light measurements vs IMPS), the performances measured for samples NB + 2h 350°C, in terms of durability and charge injection efficiency @ 1.5 V vs RHE, can be considered satisfactory.

■ CONCLUSIONS

This paper has reported on the hydrothermal fabrication of copper vanadate systems on FTO substrates and on their functionalization with CoO_x overlayers by RF-Sputtering, in view of eventual application as anodes for PEC water splitting processes. Beside a multi-technique characterization with the aid of complementary analytical tools, IMPS, a powerful technique to probe the photo-charge dynamics in the material and attain valuable mechanistic information, was used to elucidate the role of cobalt oxide overlayers.

A suitable choice of the processing conditions enabled to obtain CuV_2O_6 high-surface area NBs, whose morphology is almost preserved after CoO_x RF-sputtering. CoO_x introduction resulted in a favourable increase of material durability, a good starting point for eventual practical applications. Nevertheless, charge injection properties of the functionalized systems are rather low, due to the presence of Co^{2+} and Cu^{+} sites on material surface, as indicated by XPS characterization. These sites act as trap-states, resulting in a Fermi level pinning that, in turn, gives rise to recombination even at high band bending.

Overall, this study demonstrates how a supposedly favourable band alignment to obtain a useful *p-n* junction[42] does not necessarily yield an effective photocurrent improvement. Other factors, like interfacial ion interdiffusion and the possible occurrence of various Cu or Co oxidation states, must be also carefully considered. Future research work will be focused on the obtainment of well-defined interface between CoO_x and CuV_2O_6, eventually containing an ultrathin buffer layer (TiO_2 or HfO_2) in order to minimize interdiffusion. In this regard, different approach for the preparation of the oxide

layers (PE-CVD, sputtering or ALD) could be accompanied by a detailed transmission electron microscopy investigation to shed light into the system interfacial properties at the nanoscale level.

Associated Content

Supporting Information

Raman, photo luminescence, Mott Schottky plots and band position obtained from CuV_2O_6 NB coated by Co_3O_4 NPs (Figure S1), XRD spectra of CuV_2O_6 NB before and after thermal treatment (Figure S2), SEM images of CuV_2O_6 NB obtained with different Cu:V:PVP ratios (Figure S3), SEM images for samples NB, NB + 1h 350°C and NB + 2h 350°C and CS EDX map (Figure S4); UV-Vis spectra of the working solution after the hydrothermal synthesis (Figure S5), XPS survey scans Cu/Co and Cu/V ratio before and after PEC measurements (Figure S6), high resolution V 2p spectra of the studied samples (Figure S7), high resolution Co 2p spectra and Auger parameters of the sudied samples (Figure S8), Tauc plots of the studied samples (Figure S9), IPCE plots (Figure S10), IMPS Nyquist plots at different potentials of the studied samples (Figure S11), EQE dependence on the band bending (Figure S12), comparison of photocurrent densities and other parameters for several Cu vanadates (Table S1)

Acknowledgements

This work was partially supported by the following projects: Italian MIUR (PRIN, SMARTNESS, 2015K7FZLH, PRIN, MULTI-E, 20179337R7), and MAECI Italy-China bilateral project (GINSENG, PGR00953). D.B. and C.M. acknowledge financial support from Padova University P-DiSC #03BIRD2018-UNIPD OXYGENA project. The authors are grateful to Dr. Gregorio Bottaro (CNR-ICMATE, Padova, Italy) for acquiring photoluminescence spectra.

References

(1) Lee, D. K.; Lee, D.; Lumley, M. A.; Choi, K.; Lee, D. K. Progress on Ternary Oxide-Based Photoanodes for Use in Photoelectrochemical Cells for Solar Water Splitting. *Chem. Soc. Rev.* **2019**, *4*, 2126–2157.

(2) He, H.; Liao, A.; Guo, W.; Luo, W.; Zhou, Y.; Zou, Z. State-of-the-Art Progress in the Use of Ternary Metal Oxides as Photoelectrode Materials for Water Splitting and Organic Synthesis. *Nano Today* **2019**, *28*, 100763.

(3) Yamakata, A.; Ishibashi, T. A.; Onishi, H. Kinetics of the Photocatalytic Water-Splitting Reaction on TiO_2 and Pt/TiO_2 Studied by Time-Resolved Infrared Absorption Spectroscopy. *J. Mol. Catal. A Chem.* **2003**, *199* (1–2), 85–94.

(4) Sivula, K.; Formal, F. Le; Grätzel, M. Solar Water Splitting : Progress Using Hematite (α-Fe_2O_3) Photoelectrodes. *ChemSusChem* **2011**, *4*, 432–449.

(5) Warwick, M. E. A.; Kaunisto, K.; Barreca, D.; Carraro, G.; Gasparotto, A.; Maccato, C.; Bontempi, E.; Sada, C.; Ruoko, T.; Turner, S. Vapor Phase Processing of α-Fe_2O_3 Photoelectrodes for Water Splitting: An Insight into the Structure/Property Interplay. *ACS Appl. Mater. Interfacespplied Mater. Interfaces* **2015**, *7*, 8667–8676.

(6) Chen, Q.; Li, J.; Li, X.; Huang, K.; Zhou, B.; Cai, W.; Shangguan, W. Visible-Light Responsive Photocatalytic Fuel Cell Based on WO_3/W Photoanode and Cu_2O/Cu Photocathode for Simultaneous Wastewater Treatment and Electricity Generation. *Environ. Sci. Technol.* **2012**, *46* (20), 11451–11458.

(7) Rettie, A. J. E.; Mozaffari, S.; McDaniel, M. D.; Pearson, K. N.; Ekerdt, J. G.; Markert, J. T.; Mullins, C. B. Pulsed Laser Deposition of Epitaxial and Polycrystalline Bismuth Vanadate Thin Films. *J. Phys. Chem. C* **2014**, *118* (46), 26543–26550.

(8) Warwick, M. E. A.; Barreca, D.; Bontempi, E.; Carraro, G.; Gasparotto, A.; Maccato, C.; Kaunisto, K.; Ruoko, T.-P.; Lemmentyinen, H.; Sada, C.; Gönüllü, Y.; Mathur, S. Pt-Functionalized Fe_2O_3 Photoanodes for Solar Water Splitting: The Role of Hematite Nano-Organization and the Platinum Redox State. *Phys. Chem. Chem. Phys.* **2015**, *17*, 12899–12907.

(9) Barreca, D.; Carraro, G.; Gasparotto, A.; Maccato, C. *Metal Oxide Electrodes for Photo-Activated Water Splitting*; Elsevier Ltd., 2018.

(10) van de Krol, R. *Photoelectrochemical Hydrogen Production*; Van De Krol, R., Gärtzel, M., Eds.; Springer US, 2012.

(11) Zachäus, C.; Abdi, F. F.; Peter, L. M.; van de Krol, R. Photocurrent of $BiVO_4$ Is Limited by Surface Recombination, Not Surface Catalysis. *Chem. Sci.* **2017**, *8* (5), 3712–3719.

(12) Peng, Q.; Shan, B.; Wen, Y.; Chen, R. Enhanced Charge Transport of $LaFeO_3$ via Transition Metal (Mn , Co , Cu) Doping for Visible Light Photoelectrochemical Water Oxidation. *Int. J. Hydrogen Energy* **2015**, *40* (45), 15423–15431.

(13) Huai, X.; Girardi, L.; Lu, R.; Gao, S.; Zhao, Y.; Ling, Y.; Andrea, G.; Granozzi, G.; Zhang, Z. Nano Energy The Mechanism of Concentric $HfO_2/Co_3O_4/TiO_2$ Nanotubes Investigated by Intensity Modulated Photocurrent Spectroscopy (IMPS) and Electrochemical Impedance Spectroscopy (EIS) for Photoelectrochemical Activity. *Nano Energy* **2019**, *65* , 104020.

(14) Ng, Y. H.; Iwase, A.; Kudo, A.; Amal, R. Reducing Graphene Oxide on a Visible-Light $BiVO_4$ Photocatalyst for an Enhanced Photoelectrochemical Water Splitting. *J. Phys. Chem. Lett.* **2010**, *1* (17), 2607–2612.

(15) Shuang, S.; Girardi, L.; Rizzi, G.; Sartorel, A.; Marega, C.; Zhang, Z.; Granozzi, G. Visible Light Driven Photoanodes for Water Oxidation Based on Novel R-GO/β-$Cu_2V_2O_7/TiO_2$ Nanorods Composites. *Nanomaterials* **2018**, *8* (7), 544.

(16) Zhou, X.; Liu, R.; Sun, K.; Papadantonakis, K. M.; Brunschwig, B. S.; Lewis, N. S. 570 mV Photovoltage, Stabilized n-Si/CoO_x Heterojunction Photoanodes Fabricated Using Atomic Layer Deposition. *Energy Environ. Sci.* **2016**, *9* (3), 892–897.

(17) Carraro, G.; Maccato, C.; Gasparotto, A.; Kaunisto, K.; Sada, C.; Barreca, D. Plasma-Assisted Fabrication of Fe_2O_3 - Co_3O_4 Nanomaterials as Anodes for Photoelectrochemical Water Splitting. *Plasma Process Polym.* **2016**, *13*, 191–200.

(18) Chang, X.; Wang, T.; Zhang, P.; Zhang, J.; Li, A.; Gong, J. Enhanced Surface Reaction Kinetics and Charge Separation of p–n Heterojunction $Co_3O_4/BiVO_4$ Photoanodes. *J. Am. Chem. Soc.* **2015**, *137* (26), 8356–8359.

(19) Jiang, C.-M.; Segev, G.; Hess, L. H.; Liu, G.; Zaborski, G.; Toma, F. M.; Cooper, J. K.; Sharp, I. D. Composition-Dependent Functionality of Copper Vanadate Photoanodes. *ACS Appl. Mater. Interfaces* **2018**, *10 (13)*, 10627-10633

(20) Zhou, L.; Yan, Q.; Yu, J.; Jones, R. J. R.; Becerra-Stasiewicz, N.; Suram, S. K.; Shinde, A.;

Guevarra, D.; Neaton, J. B.; Persson, K. A.; Gregoire, J. M. Stability and Self-Passivation of Copper Vanadate Photoanodes under Chemical, Electrochemical, and Photoelectrochemical Operation. *Phys. Chem. Chem. Phys.* **2016**, *18* (14), 9349–9352.

(21) Guo, W.; Chemelewski, W. D.; Mabayoje, O.; Xiao, P.; Zhang, Y.; Mullins, C. B. Synthesis and Characterization of CuV_2O_6 and $Cu_2V_2O_7$: Two Photoanode Candidates for Photoelectrochemical Water Oxidation. *J. Phys. Chem. C* **2015**, *119* (49), 27220–27227.

(22) Carraro, G.; Maccato, C.; Gasparotto, A.; Warwick, M. E. A.; Sada, C.; Turner, S.; Bazzo, A.; Andreu, T.; Pliekhova, O.; Korte, D.; Štangar, U. L.; Tendeloo, G. Van; Morante, J. R.; Barreca, D. Hematite-Based Nanocomposites for Light-Activated Applications: Synergistic Role of TiO_2 and Au Introduction. *Sol. Energy Mater. Sol. Cells* **2020**, *159* (September 2016), 456–466.

(23) Peter, L. M. Dynamic Aspects of Semiconductor Photoelectrochemistry. *Chem. Rev.* **1990**, *90*, 753–769.

(24) E.A. Ponoamarev, L. . P. A Generalized Theory of Intensity Modulated Photocurrent Spectroscopy (IMPS). **1995**, *396*, 219–226.

(25) Yeh, J. J.; Lindau, I. Atomic Subshell Photoionization Cross Sections and Asymmetry Parameters: $1 \leq Z \leq 103$. *At. Data Nucl. Data Tables* **1985**, *32*, 1–155.

(26) PANalytial B.V. HighScore Plus. PANalytial B.V.: Almelo 2012.

(27) Kwolek, P.; Szaciłowski, K. Photoelectrochemistry of N-Type Bismuth Oxyiodide. *Electrochim. Acta* **2013**, *104*, 448–453.

(28) van de Krol, R.; Liang, Y.; Schoonman, J. Solar Hydrogen Production with Nanostructured Metal Oxides †. *J. Mater. Chem.* **2008**, *18*, 2311–2320.

(29) Pan, Z. W.; Dai, Z. R.; Wang, Z. L. Nanobelts of Semiconducting Oxides. *Science (80).* **2001**, *291*, 1947–1950.

(30) Wei, Y. J.; Wan, K.; Chen, G.; Wan, C.; Bum, K. Synthesis and Structural Properties of Stoichiometric and Oxygen Deficient CuV_2O_6 Prepared via Co-Precipitation Method. **2005**, *176*, 2243–2249.

(31) JCPDS-International Centre for Diffraction Data. PDF-# 74–2117. **1998**.

(32) JCPDS-International Centre for Diffraction Data. PDF # 73-1032. **1998**.

(33) Han, G. hong; Yang, S. zhen; Huang, Y. fang; Yang, J.; Chai, W. cui; Zhang, R.; Chen, D. liang. Hydrothermal Synthesis and Electrochemical Sensing Properties of Copper Vanadate Nanocrystals with Controlled Morphologies. *Trans. Nonferrous Met. Soc. China* **2017**, *27* (5), 1105–1116.

(34) Kosmala, T.; Calvillo, L.; Agnoli, S.; Granozzi, G. Enhancing the Oxygen Electroreduction Activity through Electron Tunnelling : CoO x Ultrathin Films on Pd (100). *ACS Catal.* **2018**, *8*, 2343–2352.

(35) Moretti, G. Auger Parameter and Wagner Plot in the Characterization of Chemical States by X-ray Photoelectron Spectroscopy : A Review. *J. Electron Spectros. Relat. Phenomena* **1998**, *95*, 95–144.

(36) Haber, J.; Ungier, L. On Chemical Shifts of ESCA and Auger Lines in Cobalt Oxides. *J. Electron Spectros. Relat. Phenomena* **1977**, *12*, 305–312.

(37) Guijarro, N.; Bornoz, P.; Prévot, M.; Yu, X.; Zhu, X.; Johnson, M.; Jeanbourquin, X.; Le Formal, F.; Sivula, K. Evaluating Spinel Ferrites MFe2O4 (M = Cu, Mg, Zn) as Photoanodes for Solar Water Oxidation: Prospects and Limitations. *Sustain. Energy Fuels* **2018**, *2* (1), 103–117.

(38) Kafi, F. S. B.; Jayathileka, K. M. D. C.; Wijesundera, R. P.; Siripala, W. Fermi-Level Pinning and Effect of Deposition Bath PH on the Fl at-Band Potential of Electrodeposited n-Cu_2O in an Aqueous Electrolyte. *Phys. Status Solidi* **2016**, *253* (10), 1965–1969.

(39) Iandolo, B.; Wickman, B.; Zori, I.; Anders Hellman. The Rise of Hematite: Origin and Strategies to Reduce the High Onset Potential for the Oxygen Evolution Reaction. *J. Mater. Chem. A* **2015**, *3*, 16896–16912.

(40) Shannon, R. D. Revised Effective Ionic Radii and Systematic Studies of Interatomie Distances in Halides and Chaleogenides. *Acta Crystallogr. Sect. A* **1976**, *A32*, 751–767.

(41) Thorne, J. E.; Jang, J.; Liu, E. Y.; Wang, D. Understanding the Origin of Photoelectrode Performance Enhancement by Probing Surface Kinetics. *Chem. Sci.* **2016**, *7*, 3347–3354.

(42) Neamen, D. A. *Additional Semiconductor Devices and Device Concepts. An Introduction to Semiconductor Devices*, Internatio.; McGraw-Hill: New York, 2006.

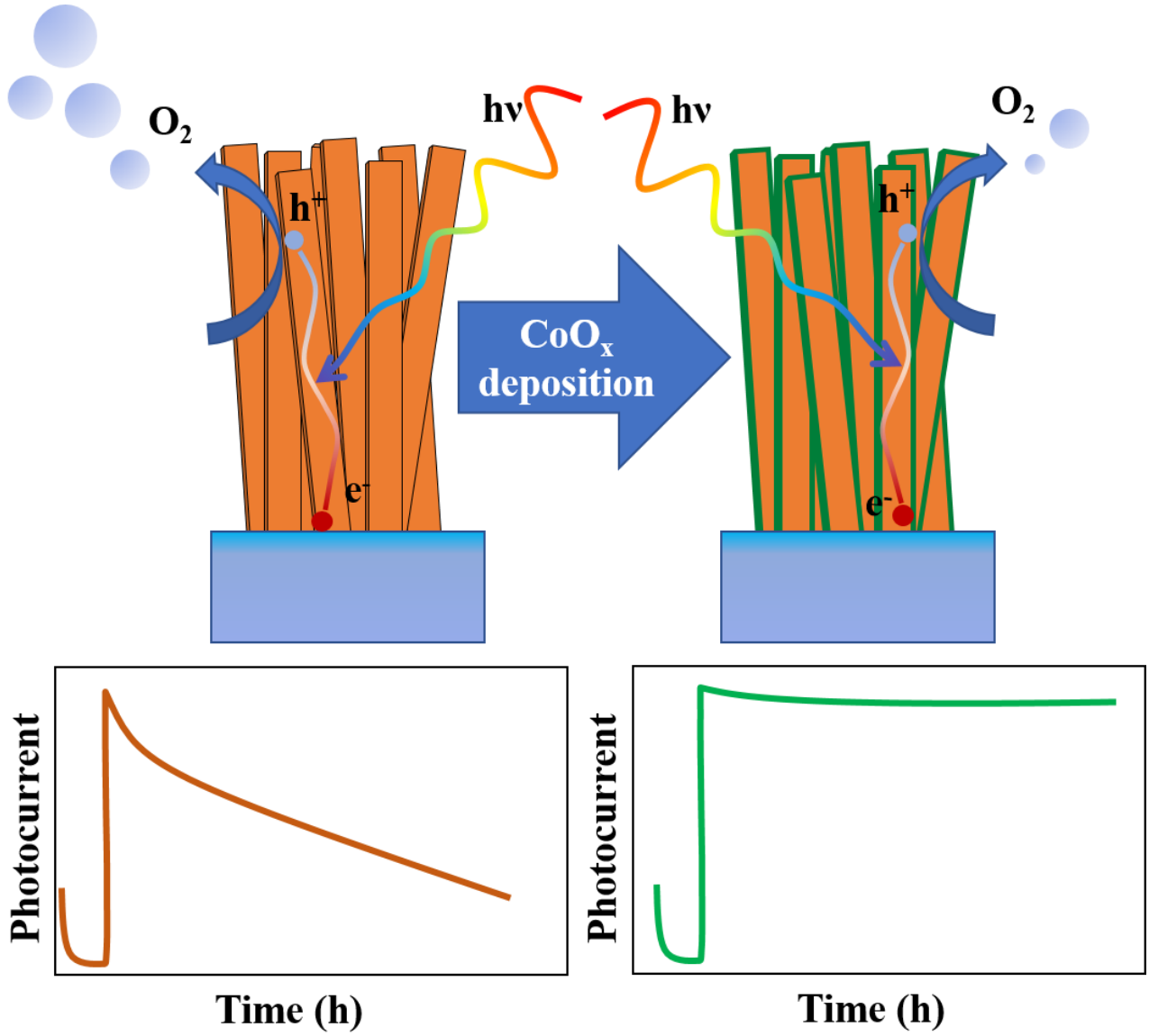

Graphical Abstract